

Multiscale aggregating discontinuities: A method for circumventing loss of material stability

Ted Belytschko^{1,*},[†],[‡], Stefan Loehnert^{2,§} and Jeong-Hoon Song^{1,¶}

¹*Theoretical and Applied Mechanics, Northwestern University, 2145 Sheridan Road, Evanston, IL 60208-3111, U.S.A.*

²*Institute of Mechanics and Computational Mechanics, Leibniz University Hannover, Appelstr. 9A, 30167 Hannover, Germany*

SUMMARY

New methods for the analysis of failure by multiscale methods that invoke unit cells to obtain the subscale response are described. These methods, called multiscale aggregating discontinuities, are based on the concept of ‘perforated’ unit cells, which exclude subdomains that are unstable, i.e. exhibit loss of material stability. Using this concept, it is possible to compute an equivalent discontinuity at the coarser scale, including both the direction of the discontinuity and the magnitude of the jump. These variables are then passed to the coarse-scale model along with the stress in the unit cell. The discontinuity is injected at the coarser scale by the extended finite element method. Analysis of the procedure shows that the method is consistent in power and yields a bulk stress–strain response that is stable. Applications of this procedure to crack growth in heterogeneous materials are given. Copyright © 2007 John Wiley & Sons, Ltd.

Received 25 June 2007; Accepted 25 June 2007

KEY WORDS: multiscale; fracture; discontinuity; finite elements; extended finite element method

1. INTRODUCTION

Multiscale methods based on unit cells, often called FE² methods [1, 2], are becoming of increasing importance because of their ability to compute the effective properties of complex microstructures on the fly. For example, the modeling of the response of composite material structures is streamlined

*Correspondence to: Ted Belytschko, Mechanical Engineering, Northwestern University, 2145 Sheridan Road, Evanston, IL 60208-3111, U.S.A.

[†]E-mail: tedbelytschko@northwestern.edu

[‡]Walter P. Murphy and McCormick Professor.

[§]Research Associate.

[¶]Graduate Research Assistant.

Contract/grant sponsor: Army Office of Scientific Research; contract/grant number: W911-NF-05-1-0049

Contract/grant sponsor: Office of Naval Research; contract/grant number: N00014-06-1-0380

considerably by such methods, since the necessity for obtaining homogenized material properties is avoided. However, the application of these methods to problems of failure still poses major difficulties, for the modeling of failure is inextricably interwoven with the loss of material stability of the constitutive law in rate-independent materials; even in rate-dependent materials, failure results in extreme localization of deformation at the macroscale, which is difficult to treat in multiscale methods.

In this paper, we describe an FE^2 multiscale method wherein the difficulties due to loss of ellipticity are circumvented by injecting discontinuities at the coarser scales when the subscale models predicts material instabilities. The method is quite natural: by means of special unit cells called ‘perforated unit cells’, we develop a method for separating the deformation corresponding to material failure from the bulk deformation. We then find an equivalent discontinuity or several discontinuities. These discontinuities are injected into the coarser-scale model; their orientation and magnitude are obtained from the same analysis. Because the method aggregates many discontinuities in the unit cell into a single discontinuity at the coarser scale, we call this method multiscale aggregating discontinuities (MAD).

We show here that this approach guarantees the material stability of the coarser-scale model. In other words, by extracting a discontinuity from the overall deformation of a unit cell, the remaining bulk material, with certain stipulations, can be shown to remain stable. Thus, the coarse-scale model remains well posed (broadly speaking) and there are no difficulties associated with mesh sensitivity.

In some works, loss of material stability has been dealt with by resorting to gradient methods to regularize the material model, e.g. Kouznetsova *et al.* [3] and McVeigh *et al.* [4]. Interesting studies on representative volume elements are given by Gitman [5] and Gitman *et al.* [6]. Oskay and Fish [7] have treated the homogenization of failure by eigendeformation techniques that bear a resemblance to the method proposed here.

Gradient and non-local models for regularizing loss of ellipticity were proposed almost 25 years ago by Bažant *et al.* [8], Triantafyllidis and Aifantis [9], and Lasry and Belytschko [10]. These developments ensued from the discovery that upon loss of ellipticity, deformation in a body localizes to a set of measure zero [11, 12] which leads to spurious behavior in numerical models, and to severe mesh dependence of the solution. Recently, regularization methods have been the topic of considerable research, and improved theories, particularly methods suitable for plasticity, have been developed, Fleck and Hutchinson [13, 14] and Gao *et al.* [15] are two of the many examples. Regularization of the standard continuum mechanics formulation may be a viable approach to circumvent loss of material stability, but it entails using non-standard finite element programs and is often quite expensive. Furthermore, determination of the degree of regularization from experiments and information passing to coarser scales poses difficulties for these methods. For example, in metals, there is little evidence that gradient models give an accurate model of plastic deformation for scales larger than the nanoscale.

The theory and application of methods for dealing with instabilities without regularization have been addressed infrequently. Abeyaratne and Triantafyllidis [16] showed that unit elastomers with periodic holes lose rank-one ellipticity even though the elastomer possessed rank-one ellipticity. Geymonat *et al.* [17] were among the first to study the loss of stability at the microscale and its implications. They examined the homogenization of a layered composite bar and determined the conditions for the loss of rank-one convexity using a Bloch wave analysis. They identified what they called short-wavelength and long-wavelength instabilities, though it should be noted that with the loss of rank-one convexity, instability occurs at all wavelengths. Müller [18] studied the issue of convexity of unit cells in a similar context. Miehe *et al.* [19] in an interesting study, developed

a theoretical framework and computational procedure that links unstable unit cells to the macroscale in a composite.

2. PRELIMINARIES

We will use a standard continuum mechanics formulation at each scale, although at the finest scale discrete methods such as atomistic or discrete element methods (DEMs) can be used (they are discussed in a subsequent paper). The motion at each scale K is given by

$$\mathbf{x} = \boldsymbol{\phi}^K(\mathbf{X}, t) \quad (1)$$

where \mathbf{x} denote the spatial coordinates and \mathbf{X} the material coordinates. The deformation gradient \mathbf{F}^K , henceforth called simply the strain, is given locally in terms of $\boldsymbol{\phi}^K$ by

$$\mathbf{F}^K = \nabla \otimes \boldsymbol{\phi}^K \quad (2)$$

where ∇ is the gradient operator in the material coordinates.

At each scale, the motion is governed by the equations of equilibrium

$$\text{DIV } \mathbf{P}^K = \mathbf{0} \quad \text{or} \quad \frac{\partial P_{ij}^K}{\partial X_j} = 0_i \quad (3)$$

where \mathbf{P} is the first Piola–Kirchhoff stress, henceforth called simply the stress, and DIV is the divergence operator; see Belytschko *et al.* [20] for a text-book account (in [20], the symbol \mathbf{P} is used for the nominal stress tensor, which is the transpose of the first Piola–Kirchhoff stress tensor). Body forces are not treated here, although including them does not pose fundamental difficulties. The displacements are given by

$$\mathbf{u}^K(\mathbf{X}, t) = \boldsymbol{\phi}^K(\mathbf{X}, t) - \mathbf{X} \quad (4)$$

The constitutive law is taken to be of the form

$$\mathbf{P}^K = \mathbf{P}^K(\mathbf{F}^K) \quad \text{or} \quad \mathbf{P}^K = \frac{\partial W}{\partial \mathbf{F}^K} \quad (5)$$

where the second equation is applicable when the material deformation is reversible so that the material possesses a potential W . We will sometimes need a tangent relationship for the constitutive law, which we write as

$$\dot{\mathbf{P}}^K = \mathcal{C}^K : \dot{\mathbf{F}}^K \quad (6)$$

where \mathcal{C}^K is the tangent modulus given by

$$\mathcal{C}^K = \frac{\partial^2 W}{\partial \mathbf{F}^K \partial \mathbf{F}^K} \quad (7)$$

and superposed dots denote material derivatives with respect to time or a time-like variable.

Our conception of the energy of the system requires some explanation. We assume that the intrinsic energy of the body is independent of the scale. The scale dependence of the material

constants arises from the resolution of the numerical method at each scale, which results in differences in the fields $\mathbf{F}^K(\mathbf{X}, t)$.

The solutions reported here have been obtained by the extended finite element method (XFEM). The displacement field at scale K is given by

$$\mathbf{u}^K(\mathbf{X}, t) = \mathbf{u}_c^K(\mathbf{X}, t) + \mathbf{u}_d^K(\mathbf{X}, t) \quad (8)$$

where \mathbf{u}_c^K is the continuous part of the displacement field and \mathbf{u}_d^K the discontinuous part. The finite element approximations for these fields in the XFEM setting are

$$\mathbf{u}_c^K(\mathbf{X}, t) = \sum_{I \in \mathcal{S}} \mathbf{u}_I^K(t) \phi_I(\mathbf{X}) \quad (9)$$

$$\mathbf{u}_d^K(\mathbf{X}, t) = \sum_{I \in \mathcal{S}_d} \mathbf{q}_I^K(t) \phi_I(\mathbf{X}) (H_\Gamma(\mathbf{X}) - H_\Gamma(\mathbf{X}_I)) \quad (10)$$

where \mathcal{S} is the set of nodes in the model, \mathcal{S}_d the set of nodes of elements crossed by a discontinuity (see, Moës *et al.* [21]), \mathbf{u}_I^K the nodal displacements, ϕ_I the shape functions, and H_Γ a step function on the discontinuity Γ^c . The enriched variables \mathbf{q}_I^K are set by the magnitude of the discontinuity obtained from the subscale solution. The XFEM method was developed in [21, 22]; recent developments are given in [23–29].

3. UNIT CELL AND INFORMATION TRANSFER

We consider a unit cell with sides of length $l = \alpha h$, where h is the characteristic element size where the unit cell is applied and α is a parameter close to unity. In the unit cell, neither the geometry nor the response is assumed to be periodic. Therefore, the localization that accompanies microcrack growth, shear band formation, and other damage modes can be treated even though such behavior is not periodic. The role of the unit cells is to provide the stress response for the coarse-scale model. In addition, they must provide the orientation and the magnitude of the displacement discontinuities.

The schema for the method is shown in Figure 1. Each subdomain in the macromodel (usually only the critical subdomains, called ‘hot spots’, are linked to unit cells), is linked with a virtual

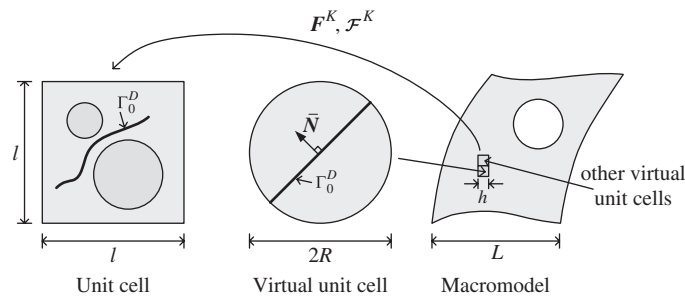


Figure 1. Schema of the multiscale aggregating discontinuities method.

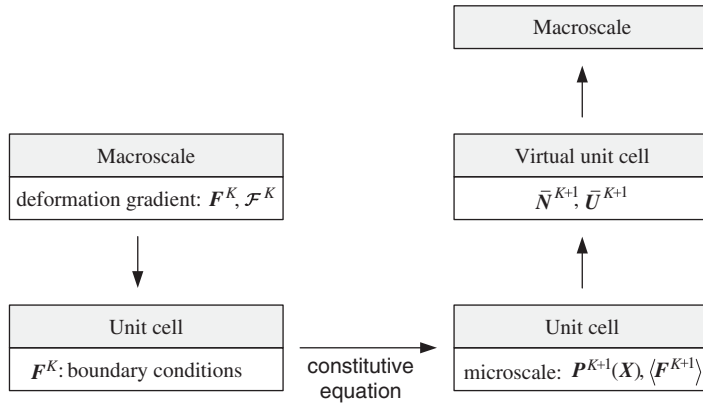


Figure 2. Flow chart of the multiscale aggregating discontinuities method.

unit cell, which in turn interrogates the actual unit cell. A point in the subdomain of the coarse-scale model is selected to be the source and recipient of the information procured at the finer scale. Usually, the subdomain is an element in a mesh and the linkage point is a Gauss quadrature point of a finite element. The procedure is usually strain driven; the effective strain \mathcal{F}^K at the point in the macroelement is applied to the unit cell as a displacement boundary condition on the edges of the unit cell. The effective strain includes both the bulk strain \mathbf{F}^K and the effect of discontinuities. However, displacement-driven unit cells often encounter certain difficulties in the treatment of localization; these, along with some remedies, are described later.

From the solution of the unit cell, the following information is obtained:

- (i) The stress at the coarser scale.
- (ii) The orientation of the effective discontinuity (or discontinuities), and, in some cases, the displacement jump across this discontinuity (or discontinuities).

The virtual unit cell in two dimensions is considered to be circular with radius $R = l/\sqrt{\pi}$ so that its area is equivalent to that of the unit cell. The role of the virtual unit cell is to provide energetic consistency of the effective discontinuity. The unit cell does not provide information on the location of the discontinuities within the associated coarse-scale subdomain, but provides information only on the orientation of the discontinuity.

Remark

While the insertion of the macro-discontinuity is usually triggered by loss of material stability, the technique is also applicable to situations where localization occurs due to a localized load.

We next describe the procedure and the micro/macro linkage with Figure 2 as a guide. As can be seen, at each sampling point at the coarser scale, the effective strain \mathcal{F}^K at scale K ($K \geq 1$) is provided by the coarse-scale computation. The boundary condition is then applied to the unit cell

$$\phi^{K+1}(\partial\Omega^{K+1}) = \mathcal{F}^K \cdot \mathbf{X} \tag{11}$$

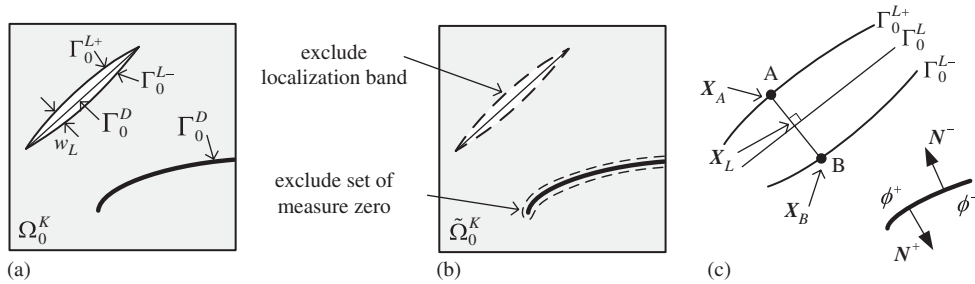


Figure 3. Representation of unit cells that contain discontinuities and localization bands: (a) unit cell Ω_0^K at scale K , (b) perforated unit cell $\tilde{\Omega}_0^K$; cracks are also excluded from the domain; and (c) definition of discontinuities and localization band geometries.

This is the standard way for prescribing the boundary motion of unit cell. The effective strain \mathcal{F}^K includes both the bulk strain \mathbf{F}^K and the discontinuous/localized deformation \mathbf{F}_E^K ; the latter can be considered as an eigenstrain and relation to the discontinuous motion is discussed later. The effective strain is similar to a gauge strain, i.e. it is an average strain over a finite subdomain. Discontinuities at scale K are included in the effective strain; the bulk strain \mathbf{F}^K is the continuous deformation at scale K .

The above is called the ‘localization step’ by Feyel and Chaboche [1], but we do not call this process ‘localization’ since we use this term for ‘localization of deformation’. It links a more detailed subscale model with the coarse-grained model.

The response of the unit cell is then computed using the constitutive laws of the microconstituents. Note that these constitutive laws can include a crack growth law or crack nucleation and propagation laws.

The two scales are linked through averaging methods that are characteristic of unit cell methods. The notable feature of the proposed method is that the averaging operation excludes all subdomains in the unit cell that exhibits material instabilities; this includes both nucleating and growing cracks and other manifestations of material instability such as shear bands. For cracks, the entire crack is excluded. An example of such a unit cell is shown in Figure 3. We call the unit cell with ‘holes’ around domains of material instabilities a ‘perforated’ unit cell. Note that the domains excluded around cracks are sets of measure zero, i.e. lines in two dimensions and surfaces in three dimensions.

Consider a unit cell such as shown in Figure 3(a). It contains a discontinuity Γ_0^D and a localization band Ω_0^L . It is assumed that the width of the localization band, denoted by w_L , is small compared with the dimensions of the cell e . The edges of the localization band are denoted by Γ_0^{L+} and Γ_0^{L-} , the midline by Γ_0^L . We denote the domain of the perforated unit cell by $\tilde{\Omega}_0 = \Omega_0 \setminus (\Omega_0^L \cup \Gamma_0^D)$. For simplicity, we consider a single localization band and a single discontinuity in the following, but the extension to multiple cracks and localization bands is straightforward.

The averaging operation for any function $f(\mathbf{X})$ is defined by

$$\langle f^K \rangle = \frac{1}{|\tilde{\Omega}_0^K|} \int_{\tilde{\Omega}_0^K} f^K \, d\Omega \tag{12}$$

where $|\cdot|$ denotes the measure of the domain, which is the area in two dimensions and the volume in three dimensions. Note that, in contrast to standard methods, the averaging operation is over the perforated domain.

The average bulk strain at scale K is given by

$$\langle \mathbf{F}^K \rangle = \frac{1}{|\tilde{\Omega}_0^K|} \int_{\tilde{\Omega}_0^K} \mathbf{F}^K \, d\Omega \tag{13}$$

We define the bulk strain at scale $K - 1$ to be the average strain at scale K , hence

$$\mathbf{F}^{K-1} \equiv \langle \mathbf{F}^K \rangle \tag{14}$$

The average stress is defined similarly as

$$\langle \mathbf{P}^K \rangle = \frac{1}{|\tilde{\Omega}_0^K|} \int_{\tilde{\Omega}_0^K} \mathbf{P}^K \, d\Omega \equiv \mathbf{P}^{K-1} \tag{15}$$

and, as indicated, gives the stress at the coarser scale.

A crucial step in this theory is the determination of the discontinuity or discontinuities at scale $K - 1$ emanating from the response of the unit cell at scale K . It would be desirable to establish a single discontinuity from the difference between the effective strain at scale $K - 1$ and the average strain at scale K (which corresponds to the bulk strain at scale $K - 1$), i.e. to find a normal $\tilde{\mathbf{N}}$ such that

$$\tilde{\mathbf{U}}^{K-1} \otimes \tilde{\mathbf{N}}^{K-1} = \mathcal{F}^{K-1} - \langle \mathbf{F}^K \rangle \equiv \mathcal{F}^{K-1} - \mathbf{F}^{K-1} \tag{16}$$

where $\tilde{\mathbf{U}}$ is a non-dimensional displacement jump that is related to the displacement discontinuity at scale $K - 1$ by

$$[[\mathbf{u}^{K-1}]] = [[\boldsymbol{\phi}^{K-1}]] = \frac{|\tilde{\Omega}_0^K|}{R} \tilde{\mathbf{U}}^{K-1} \tag{17}$$

where $[[\boldsymbol{\phi}^{K-1}]]$ is the jump in $\boldsymbol{\phi}(\mathbf{X}, t)$ at scale $K - 1$ at the position of the unit cell, and R is the radius of the virtual unit cell in two dimensions. We use the following convention for defining a jump (see Figure 3):

$$[[\boldsymbol{\phi} \otimes \mathbf{N}]] = \boldsymbol{\phi}^+ \mathbf{N}^- + \boldsymbol{\phi}^- \mathbf{N}^+ \tag{18}$$

such that for a crack the jump is positive in the crack-opening mode, where \mathbf{N} is the normal in the reference configuration.

However, the left-hand side of Equation (16) is a rank-one tensor, whereas the right-hand side is usually a rank-three tensor. In general, a jump $\tilde{\mathbf{U}}^{K-1}$ and a normal $\tilde{\mathbf{N}}^{K-1}$ that satisfy Equation (16)

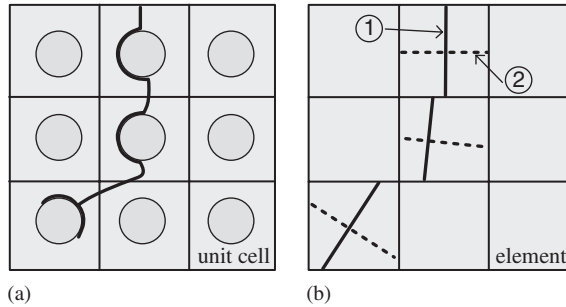


Figure 4. (a) A crack path through a composite based on microstructural analysis and (b) the corresponding dual discontinuity configuration; dark bold lines denote primary discontinuities $\bar{\mathbf{N}}_1$ and dashes denote secondary discontinuities $\bar{\mathbf{N}}_2$.

cannot be found. Therefore, we find $\bar{\mathbf{U}}^{K-1}$ and $\bar{\mathbf{N}}^{K-1}$ by minimizing the quadratic form

$$(\bar{\mathbf{U}}^{K-1}, \bar{\mathbf{N}}^{K-1}) = \arg \left(\min_{\bar{\mathbf{U}}, \bar{\mathbf{N}}} (\bar{\mathbf{U}} \otimes \bar{\mathbf{N}} - \mathcal{F}^{K-1} + \langle \mathbf{F}^K \rangle)^2 \right) \quad (19)$$

The above provides a single discontinuity for each coarse-scale point (i.e. a Gauss quadrature point in finite elements). A simple procedure for solving (19) is given in Appendix B.

At times, it is desirable to introduce more than one discontinuity at each point. For example, when a crack progresses in a composite as shown in Figure 4(a), then an appropriate crack pattern is that in Figure 4(b). Basically, because of the complexity of the crack path in the unit cells, a single discontinuity in each element may not suffice to adequately represent subscale behavior. By using two discontinuities for each unit cell, a better representation of subscale behavior can be obtained.

Multiple discontinuities are injected as follows. First, we find $\bar{\mathbf{U}}_1^{K-1}$ and $\bar{\mathbf{N}}_1^{K-1}$ by Equation (19). We then construct $\bar{\mathbf{N}}_2^{K-1}$ (and $\bar{\mathbf{N}}_3^{K-1}$ in three dimensions) by orthogonalizing them to $\bar{\mathbf{N}}_1^{K-1}$ (and $\bar{\mathbf{N}}_2^{K-1}$). The jumps $\bar{\mathbf{U}}_\alpha^{K-1}$ can then be found by solving

$$\bar{\mathbf{U}}_\alpha^{K-1} \otimes \bar{\mathbf{N}}_\alpha^{K-1} = \mathcal{F}^{K-1} - \langle \mathbf{F}^K \rangle \equiv \mathcal{F}^{K-1} - \mathbf{F}^{K-1} \quad (20)$$

for $\bar{\mathbf{U}}_\alpha^{K-1}$, where α is the number of orthogonal discontinuities; it must equal the number of space dimensions. In the above and henceforth, the subscripted variables are summed over their range. When $\bar{\mathbf{U}}$ or $\bar{\mathbf{N}}$ appears without a subscript, it is assumed that there is only one discontinuity. Note that the surfaces of discontinuity as defined here can rotate with time.

When the traction across the discontinuity is non-vanishing, the discontinuity is injected into the coarser scale by prescribing the values of the enrichment variables \mathbf{q}^{K-1} . In our current implementation, the discontinuity magnitude is piecewise constant in the elements, so we replace $\phi_I(\mathbf{X})$ in Equation (10) by the indicator function $\zeta^e(\mathbf{X})$, where

$$\zeta^e(\mathbf{X}) = \begin{cases} 1 & \text{if } \mathbf{X} \text{ corresponds to the unit cell} \\ 0 & \text{otherwise} \end{cases} \quad (21)$$

The jump magnitude $\bar{\mathbf{U}}^{K-1}$ is related to \mathbf{q}_e^{K-1} by

$$\mathbf{q}_e^{K-1} = \frac{|\tilde{\Omega}_0^K|}{R} \bar{\mathbf{U}}^{K-1} \tag{22}$$

It is easily shown from Equations (8)–(10) that in element e the jump in the displacement is given by

$$\llbracket \mathbf{u}^{K-1} \rrbracket_\Gamma = \frac{|\tilde{\Omega}_0^K|}{R} \bar{\mathbf{U}}^{K-1} \tag{23}$$

Once the traction across the discontinuity vanishes, the magnitude of the jump is no longer prescribed. Instead, we switch to precisely the form given in Equation (10) and let the variables \mathbf{q}_l^{K-1} be unknowns in the discrete equations. The magnitude of the discontinuity then becomes piecewise continuously differentiable. A projection is used to pass from the piecewise constant to the continuously differentiable discontinuity.

The MAD method introduces a length scale into the coarse-grained model, since it implicitly provides a cohesive law by passing a stress and dislocation (for example, a crack) opening. Cohesive laws in a continuum provide a length scale through the relation between the traction and displacement jump magnitude.

The unit cell must be of the same size as the related coarse-scale element. The reason for this is explained in Appendix A.

3.1. Eigenstrain method

Another method for linking the scales is to insert an eigenstrain \mathbf{F}_E^{K-1} into the coarser scale until the unit cell loses all strength across an incipient discontinuity, i.e. until the traction $\mathbf{P} \cdot \mathbf{N}_1 = 0$, and then injecting the discontinuities. The eigenstrain is defined by a variant of Equation (16):

$$\mathbf{F}_E^{K-1} = \mathcal{F}^{K-1} - \langle \mathbf{F}^K \rangle \tag{24}$$

The difficulty with this approach is that the injection of eigenstrains is not effective in representing cracks or shear bands at the coarser scale. However, an effective technique can be developed as follows. The early part of the evolution of the failure of the unit cell is treated by Equation (24). When $\mathbf{P} \cdot \mathbf{N}_1 = 0$, we inject a discontinuity that is found by a counterpart of Equation (19):

$$(\bar{\mathbf{U}}^{K-1}, \bar{\mathbf{N}}^{K-1}) = \arg \left(\min_{\bar{\mathbf{U}}, \bar{\mathbf{N}}} (\bar{\mathbf{U}} \otimes \bar{\mathbf{N}} - \mathbf{F}_E^{K-1})^2 \right) \tag{25}$$

If it is desirable to insert more than one crack, the counterpart of Equation (20) is used. This approach bypasses difficulties associated with the rotation of the normals $\bar{\mathbf{N}}_\alpha^{K-1}$. A simple algebraic equation for the solution of the above is given in Appendix B.

3.2. Remarks on the unit cell

The perforated unit cell is crucial to the determination of the direction of the injected discontinuity at the coarser scale. At the finest scale, it is desirable that the model is regularized by one of the many models available, i.e. viscoplastic material laws, gradient models or non-local models. Alternatively, one can use an element size regularization, where the unstable part of the constitutive equation is modified so that it captures the correct fracture energy for the element in which it

occurs. The treatment of cracks at the finest scale does not require regularization if the cracks are treated as discontinuities. It should be borne in mind that the nucleation and propagation of cracks is a manifestations of unstable material behavior. However, when a critical stress or strain criterion is used to nucleate or propagate a crack, there is no need for a stability analysis.

Many criteria can be developed for identifying domains of unstable material behavior. We have used the rank-one convexity criterion and the strict ellipticity criterion. The rank-one convexity criterion is equivalent to the loss of ellipticity of the underlying PDE, so it is often called an ellipticity condition. To determine the proximity of a material point to unstable behavior by this measure, we evaluate

$$s = S(\mathcal{C}^K) \quad (26)$$

where

$$S(\mathcal{C}^K) = \min_{\mathbf{g}, \mathbf{h}} (\mathbf{g} \otimes \mathbf{h}) : \mathcal{C}^K : (\mathbf{g} \otimes \mathbf{h}) \quad (27)$$

When $s < 0$, the material is unstable. All subdomains of Ω_0^K that meet the criterion

$$s \leq s^{\text{crit}} \quad (28)$$

are then included in the localization domain Ω_0^L , where s^{crit} is a value slightly greater than zero at which we presume unstable behavior. Although premature injection of discontinuities is not fatal, tardy injection is undesirable, since it leads to an unstable material model in the corresponding coarse-grained element.

The rank-one stability criterion is expensive to check. An alternative stability criterion is the strict ellipticity criterion, which requires that

$$\dot{\mathbf{F}} : \mathcal{C}^K : \dot{\mathbf{F}} > 0 \quad \forall \dot{\mathbf{F}} \quad (29)$$

This condition is a stronger condition than the rank-one ellipticity condition. However, the discrepancy between the two is usually quite small, so it provides a useful way to construct the perforated unit cell. Equation (29) corresponds to the positive definiteness of \mathcal{C} , so it can be easily checked by computing the eigenvalues of \mathcal{C} .

Next, we discuss some basic difficulties in the treatment of unit cells with localization and cracking. In conventional unit cells with continuous deformation, when the unit cell is strain driven, the displacements are prescribed on the entire periphery of the cell. However, as shown in Figure 5, for unit cells with discontinuities, this leads to inconsistencies, when for example, a crack or shear band intersects an edge. When a shear band intersects an edge, the displacement tangential to the shear band must be discontinuous, for otherwise the shear band is terminated at the boundary. Thus, the response of the unit cell is not compatible with the prescribed linear displacements, as illustrated along the edge CD in Figure 5.

We have developed two methods for alleviating these difficulties. The first method is based on altering the prescribed displacement procedure when a discontinuity is detected in the neighborhood of a boundary. In that case, the nodes on the boundary around the anticipated path of the discontinuity are released and a traction equal to the average traction on the remaining boundary

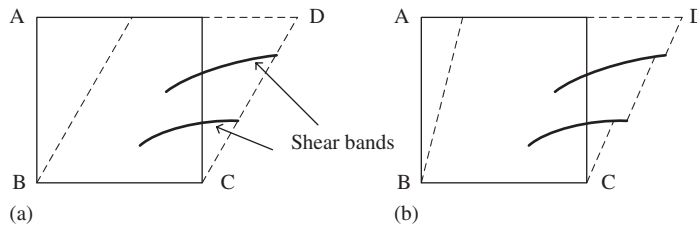


Figure 5. A perforated unit cell under pure shear with shear bands: (a) inconsistent prescribed boundary displacements and (b) consistent boundary displacements.

is applied. Though this procedure deviates from the proofs that follow, the consistency properties between the scales are not disrupted excessively.

An alternative is to use stress-driven unit cells. Although at first glance this is somewhat incompatible with the character of a displacement-based finite element method, a stress-driven approach is quite attractive when one bears in mind that

- (i) The time interval over which the unstable response occurs is usually quite small compared with the response time of the entire structure.
- (ii) It is feasible to run a displacement-driven unit cell until discontinuities or localization bands approach the boundaries, and to then switch to a stress-driven unit cell, although care must be taken to have a smooth transition.

When we use a stress-driven unit cell, it is driven iteratively so that, for the converged value $\bar{\mathbf{P}}^{K-1}$, the boundary displacements match the macrostrain at the end of the procedure, i.e.

$$\mathcal{F}^{K-1} = \langle \mathbf{F}^K \rangle + \bar{\mathbf{U}}_\alpha^{K-1} \otimes \bar{\mathbf{N}}_\alpha^{K-1} \equiv \mathbf{F}^{K-1} + \bar{\mathbf{U}}_\alpha^{K-1} \otimes \bar{\mathbf{N}}_\alpha^{K-1} \quad (30)$$

which corresponds to Equation (20). This iterative procedure can be interwoven with the iterations required in solving the $K - 1$ scale equilibrium equations.

Another alternative approach is to pre-compute the response of the perforated unit cell or to train a neural network with the perforated unit cell. Recent work [30, 31] has shown that neural networks can reproduce the constitutive response measured in experiments to a high degree of fidelity, particularly for monotonically increasing loads. In most applications of the proposed multiscale procedures, we envision that the loads are monotonic. The only extension that is needed to apply these neural network methods to the perforated unit cell is to provide additional output, namely $\bar{\mathbf{U}}_\alpha$ and $\bar{\mathbf{N}}_\alpha$. This entails only a minor complication. The use of such neural network models would tremendously speed up these multiscale analysis methods, particularly when many of the unit cells are identical.

The treatment of boundary effects of the macromodel and the failure of adjacent unit cells also require additional study. It goes without saying that a unit cell adjacent to a boundary behaves differently from a unit cell in the bulk material. For example, if edge AB in Figure 5 is a free boundary, the application of a displacement boundary condition based on \mathcal{F}^{K-1} on the edge is obviously inappropriate. Instead, such a boundary unit cell should be solved with the edge AB free; this boundary effect has already been noted by Feyel [2].

Similarly, it may be advantageous to reflect the growth of discontinuities adjacent to a unit cell in the unit cell computations. For example, if the cell to the left of the one in Figure 5

undergoes discontinuous motions, then this behavior should be reflected in the treatment of edge AB . Fortunately, failure in an adjacent cell accelerates the growth of strain in the target cell, hence this issue may not be critical.

4. INTERSCALE RELATIONS

In this section, we derive the relations between the unit cell and the coarser-grained system. The fine scale is denoted by K and the coarser scale is denoted by $K - 1$. For a two-scale analysis, $K = 1$ would be the macroscale and $K = 2$ would be the microscale.

We assume that the discontinuities and localization bands are fixed in space after they have nucleated. This is quite reasonable for cracks and shear bands, because after shear bands or cracks nucleate and evolve their configurations are frozen. We also assume, without loss of generality, that the entities Γ_0^L and Γ_0^D are independent of time and known *a priori* for the purposes of this analysis. Finally, we assume that the stress is everywhere bounded and that $\llbracket \boldsymbol{\phi}^K \otimes \mathbf{N} \rrbracket$ is a continuously differentiable function along $\Gamma_0^L \cup \Gamma_0^D$; this assumption precludes elastic traction-free cracks.

It is assumed that for every point \mathbf{X}^L of the midline on the localization band Γ_0^L there exist a pair of points \mathbf{X}_{L+} and \mathbf{X}_{L-} on Γ_0^{L+} and Γ_0^{L-} , respectively (see Figure 3(c)), such that

$$\mathbf{X}_L = \frac{1}{2}(\mathbf{X}_A + \mathbf{X}_B) \quad (31)$$

and that the lines AB between points \mathbf{X}_A and \mathbf{X}_B are approximately normal to Γ_0^L . It is also assumed that the tractions $\mathbf{P}^K \cdot \mathbf{N}^K$ are approximately constant in Ω_0^L along the line AB so that

$$\llbracket \mathbf{P}^K \cdot \mathbf{N}^K \rrbracket = 0 \quad (32)$$

On any discontinuity Γ_0^D such as a crack, it follows from equilibrium that Equation (32) holds. From Gauss' theorem and Equation (32), it follows that

$$\begin{aligned} \int_{\tilde{\Omega}_0} \text{DIV } \mathbf{P} \, d\Omega &= \int_{\Gamma_0^L \cup \Gamma_0^D} \llbracket \mathbf{P} \cdot \mathbf{N} \rrbracket \, d\Omega + \int_{\partial\Omega_0} \mathbf{P} \cdot \mathbf{N} \, d\Omega \\ &= \int_{\partial\Omega_0} \mathbf{P} \cdot \mathbf{N} \, d\Omega \end{aligned} \quad (33)$$

We only analyze the prescribed boundary displacement unit cell. We first show that the average bulk strain $\langle \mathbf{F}^K \rangle$ of the unit cell is related to the effective coarse-scale strain \mathcal{F}^{K-1} (i.e. the strain prescribed to the unit cell) by

$$|\Omega_0^K| \mathcal{F}^{K-1} = |\tilde{\Omega}_0^K| \langle \mathbf{F}^K \rangle + \int_{\Gamma_0^L \cup \Gamma_0^D} \llbracket \boldsymbol{\phi}^K \otimes \mathbf{N} \rrbracket \, d\Gamma \quad (34)$$

Note that the normal is tacitly taken to be at the same scale as the preceding variable, i.e. in (34) \mathbf{N} refers to \mathbf{N}^K because it is preceded by $\boldsymbol{\phi}^K$. The above is an extension of the average strain theorem (see, Zohdi and Wriggers [32] or Nemat-Nasser and Hori [33]) previously given in Loehnert [34].

The proof is as follows. From the definition of the deformation gradient $\mathbf{F}^K = \nabla \otimes \boldsymbol{\phi}^K$, it follows that

$$\begin{aligned} |\tilde{\Omega}_0^K| \langle \mathbf{F}^K \rangle &= \int_{\tilde{\Omega}_0^K} \nabla_0 \otimes \boldsymbol{\phi}^K \, d\Omega_0 \\ &= \int_{\Gamma_0^{L+} \cup \Gamma_0^{L-}} \boldsymbol{\phi}^K \otimes \mathbf{N} \, d\Gamma + \int_{\partial\Omega_0} \boldsymbol{\phi}^K \otimes \mathbf{N} \, d\Gamma + \int_{\Gamma_0^D} \llbracket \boldsymbol{\phi}^K \otimes \mathbf{N} \rrbracket \, d\Gamma \end{aligned} \quad (35)$$

The second equality follows from Gauss' theorem. Since $w_L \ll h$, we can replace the first integral in the above using

$$\int_{\Gamma_0^{L+} \cup \Gamma_0^{L-}} \boldsymbol{\phi}^K \otimes \mathbf{N} \, d\Gamma = \int_{\Gamma_0^L} \llbracket \boldsymbol{\phi}^K \otimes \mathbf{N} \rrbracket \, d\Gamma \quad (36)$$

In the displacement-controlled procedure

$$\boldsymbol{\phi}^K = \mathcal{F}^{K-1} \cdot \mathbf{X} \quad \text{on } \partial\Omega \quad (37)$$

We can then transform the second term in Equation (35) as follows:

$$\int_{\partial\Omega_0} \boldsymbol{\phi}^K \otimes \mathbf{N} \, d\Gamma = \int_{\partial\Omega_0} (\mathcal{F}^{K-1} \cdot \mathbf{X}) \otimes \mathbf{N} \, d\Gamma = \mathcal{F}^{K-1} \cdot \int_{\partial\Omega_0} (\mathbf{X} \otimes \mathbf{N}) \, d\Gamma = |\Omega_0^K| \mathcal{F}^{K-1} \quad (38)$$

where the last equality follows from Gauss' theorem. Substituting Equations (36) and (38) into Equation (35), it follows that Equation (30) holds, which completes the proof.

It can be seen by comparing Equation (36) with Equation (34) that the injected discontinuity corresponds to a mean of the discontinuities in Γ^D and the localization band Γ^L , i.e.

$$R\bar{\mathbf{U}}^{K-1} \otimes \bar{\mathbf{N}}^{K-1} = \int_{\Gamma_0^L \cup \Gamma_0^D} \llbracket \boldsymbol{\phi}^K \otimes \mathbf{N} \rrbracket \, d\Gamma \quad (39)$$

By combining Equations (34) and (39), it follows that

$$\mathcal{F}^{K-1} = \langle \mathbf{F}^K \rangle + \beta \llbracket \boldsymbol{\phi}_\alpha^{K-1} \otimes \mathbf{N}_\alpha \rrbracket \quad (40)$$

where

$$\beta = \frac{R}{|\Omega_0^K|} \quad (41)$$

Average stress: The average stress is defined by

$$\langle \mathbf{P}^K \rangle = \frac{1}{|\tilde{\Omega}_0^K|} \int_{\tilde{\Omega}_0^K} \mathbf{P}^K \, d\Omega \quad (42)$$

We define the coarse-scale stress as

$$\mathbf{P}^{K-1} = \langle \mathbf{P}^K \rangle \quad (43)$$

For a stress-driven unit cell, the equivalence is shown as follows.

We first note that

$$\begin{aligned} \int_{\tilde{\Omega}_0^K} \text{DIV}(\mathbf{X} \otimes \mathbf{P}^K) \, d\Omega &= \int_{\tilde{\Omega}_0^K} (\mathbf{X} \cdot \text{DIV} \mathbf{P}^K + \text{DIV} \mathbf{X} \cdot \mathbf{P}^K) \, d\Omega \\ &= \int_{\tilde{\Omega}_0^K} \mathbf{P}^K \, d\Omega \quad \text{by equilibrium and } \text{DIV} \mathbf{X} = \mathbf{I} \\ &= |\tilde{\Omega}_0^K| \langle \mathbf{P}^K \rangle \end{aligned} \tag{44}$$

Applying Gauss’ theorem to the LHS of the above gives

$$\begin{aligned} \int_{\tilde{\Omega}_0^K} \text{DIV}(\mathbf{X} \otimes \mathbf{P}^K) \, d\Omega &= \int_{\partial\tilde{\Omega}_0^K} (\mathbf{X} \otimes \mathbf{P}^K) \cdot \mathbf{N} \, d\Gamma \\ &= \mathbf{P}^{K-1} : \int_{\partial\tilde{\Omega}_0^K} \mathbf{N} \otimes \mathbf{X} \, d\Gamma \\ &= \mathbf{P}^{K-1} \cdot \int_{\tilde{\Omega}_0^K} \mathbf{I} \, d\Omega = \mathbf{P}^{K-1} |\tilde{\Omega}_0^K| \end{aligned} \tag{45}$$

where the second equation follows from Gauss’ theorem. Comparing Equation (44) with (45), Equation (43) follows.

Power theorem: We next show that the power at level $K - 1$ equals the power of the unit cell. This theorem states that

$$\mathbf{P}^{K-1} : \dot{\mathcal{F}}^{K-1} = \langle \mathbf{P}^K : \dot{\mathbf{F}}^K \rangle + \frac{1}{|\tilde{\Omega}_0^K|} \int_{\Gamma_0^t \cup \Gamma_0^D} \mathbf{P}^K : \llbracket \dot{\phi}^K \otimes \mathbf{N} \rrbracket \, d\Gamma \tag{46}$$

This is an extension of Hill’s theorem; Hill’s theorem only includes the first term on the right-hand side. The proof is as follows. We note that

$$\begin{aligned} |\tilde{\Omega}_0^K| \langle \mathbf{P}^K : \dot{\mathbf{F}}^K \rangle &= \int_{\tilde{\Omega}_0^K} \mathbf{P}^K : \nabla \dot{\phi}^K \, d\Omega \\ &= \int_{\tilde{\Omega}_0^K} [\nabla \cdot (\mathbf{P}^K \cdot \dot{\phi}^K) - \dot{\phi}^K \cdot \text{DIV} \mathbf{P}^K] \, d\Omega \end{aligned} \tag{47}$$

By equilibrium, the last term vanishes and applying the divergence theorem yields

$$|\tilde{\Omega}_0^K| \langle \mathbf{P}^K : \dot{\mathbf{F}}^K \rangle = \int_{\partial\tilde{\Omega}_0^K} \mathbf{P}^K : (\dot{\phi}^K \otimes \mathbf{N}) \, d\Gamma - \int_{\Gamma_0^t \cup \Gamma_0^D} \mathbf{P}^K : \llbracket \dot{\phi}^K \otimes \mathbf{N} \rrbracket \, d\Gamma \tag{48}$$

Evaluating the first term on the RHS of Equation (48) using Equation (37) gives

$$\begin{aligned} \int_{\partial\tilde{\Omega}_0^K} \mathbf{P}^K : (\dot{\phi}^K \otimes \mathbf{N}) \, d\Omega &= \int_{\tilde{\Omega}_0^K} \text{DIV}[(\mathbf{P}^K)^T \cdot \dot{\mathcal{F}}^{K-1} \cdot \mathbf{X}] \, d\Omega \\ &= |\tilde{\Omega}_0^K| \mathbf{P}^{K-1} : \dot{\mathcal{F}}^{K-1} \end{aligned} \tag{49}$$

where the last line follows from equilibrium and Equation (43). Substituting Equation (49) into (48) and rearranging the terms gives Equation (46).

Stability: In a multiscale procedure, it is important to show that the material properties obtained from the finer scale yield a well-posed coarser-scale model. This requirement entails that the relation between $\dot{\mathbf{P}}^{K-1}$ and $\dot{\mathbf{F}}^{K-1}$ obtained from a unit cell at scale K is stable.

We show that

$$\dot{\mathbf{F}} : \mathcal{C}^{K-1} : \dot{\mathbf{F}} > 0 \quad \forall \dot{\mathbf{F}}^{K-1} \tag{50}$$

if the bulk material in the perforated unit cell $\tilde{\Omega}_0^K$ satisfies Equation (50) for all \mathcal{C}^K . Although this condition is stronger than the rank-one ellipticity condition (Equations (26)–(28)) and precludes buckling, it is adequate for our purposes because the domain of stability given by Equation (50) usually coincides closely with that given by Equations (26)–(28). In the applications we consider, buckling is not relevant.

The first steps in the proof are similar to those in the previous part, with \mathbf{P}^K replaced by $\dot{\mathbf{P}}^K$. Hence, following the steps used to obtain Equations (48) and (49), we obtain

$$|\tilde{\Omega}_0^K| \langle \dot{\mathbf{P}}^K : \dot{\mathbf{F}}^K \rangle = |\tilde{\Omega}_0^K| \dot{\mathbf{P}}^{K-1} : \dot{\mathcal{F}}^{K-1} + \int_{\Gamma_0^L \cup \Gamma_0^D} \dot{\mathbf{P}}^K : \llbracket \dot{\boldsymbol{\phi}}^K \otimes \mathbf{N} \rrbracket d\Gamma \tag{51}$$

By rearranging these terms and using $\dot{\mathbf{P}}^{K-1} = \mathcal{C}^{K-1} : \dot{\mathbf{F}}^{K-1}$, $\dot{\mathbf{P}}^K = \mathcal{C}^K : \dot{\mathbf{F}}^K$ and Equation (40), we obtain

$$\begin{aligned} \dot{\mathbf{F}}^{K-1} : \mathcal{C}^{K-1} : \dot{\mathbf{F}}^{K-1} &= \frac{1}{|\tilde{\Omega}_0^K|} \int_{\tilde{\Omega}_0^K} \dot{\mathbf{F}}^K : \mathcal{C}^K : \dot{\mathbf{F}}^K d\Omega \\ &\quad - \int_{\Gamma_0^L \cup \Gamma_0^D} \dot{\mathbf{P}}^K : \llbracket \dot{\boldsymbol{\phi}}^K \otimes \mathbf{N} \rrbracket d\Gamma \\ &\quad + \beta \dot{\mathbf{P}}^{K-1} : (\dot{\mathbf{U}}_\alpha \otimes \bar{\mathbf{N}}_\alpha + \bar{\mathbf{U}}_\alpha \otimes \dot{\mathbf{N}}_\alpha) \end{aligned} \tag{52}$$

Since all material that is unstable has been excluded from $\tilde{\Omega}_0$, the first term on the RHS is positive. The second and third terms represent the differences between the average and actual incremental dissipation and generally are close to zero. We show in the Appendix that when the unit cell is one dimensional, the bulk response is stable. Hence, when the material is stable in the perforated unit cell (domain $\tilde{\Omega}_0^K$), the material at level $K - 1$ is stable.

Stability at the macrolevel, can in any case be achieved by manipulating $\dot{\mathbf{U}}^{K-1}$. If we scale $\dot{\mathbf{U}}^{K-1}$ or β in Equation (52), so that the third term exceeds the second term, strict ellipticity is guaranteed at the macrolevel. The former corresponds to slight perturbation of the crack-opening rate at the coarser scale.

It should be noted that the above proof does not contradict the finding of Abeyaratne and Triantafyllidis [16] that a unit cell with holes is unstable even if the material remains stable. In our case, we are interested in the overall stability of the bulk material. The unstable part of the response is reflected in the discontinuity.

Note that \mathcal{C}^K , since it relates $\dot{\mathbf{P}}^K$ to $\dot{\mathbf{F}}^K$, is the first elasticity tensor. Therefore, it is a function of the current stress and can lose positive definiteness even when the material tangent stiffness is

positive definite. Thus, when buckling occurs at the fine scale, $\mathcal{C}^{K-1} < 0$ in some subdomain of the unit cell, and it is possible that $\mathcal{C}^K < 0$.

Zhodi [35] has pointed out that the above theorem is related to the Hill's comparison theorem [32, p. 59] which was developed for bounding the stiffnesses of obtaining unit cell models with irregular shapes. However, here it is used to show the relationship between stability at the two scales.

5. IMPLEMENTATION

The multiscale method can be used with any non-linear solid mechanics software. The problems we report are all two dimensional and a four-node quadrilateral with one-point quadrature element with hourglass control [36–38], with the unit cell providing the stress at the quadrature point.

The discontinuity is placed at the centroid of the element if there are no contiguous elements with discontinuities. If a discontinuity has already been inserted in a contiguous element, then the new discontinuity is inserted so that the discontinuity line is continuous. After the discontinuity has progressed several elements, situations may arise where the discontinuity is quite short. We have not carefully examined the best way to treat this. At this time, we add a second discontinuity in the element (maintaining consistency in energy). The discontinuity is then propagated into the adjacent element for which the unit cell first loses material stability. Generally, this results in unloading of adjacent elements so that only one discontinuity continues to progress.

6. NUMERICAL EXAMPLES

6.1. Computation of equivalent discontinuity

We illustrate first the application of the coarse-graining procedure to a unit cell with multiple fatigue crack growth. As can be seen from Figure 6, when a single crack is used to coarse grain the fine-scale solution, the crack rotates in a counterclockwise direction for the configurations shown. In the final configuration, percolation has occurred and the coarse-grain crack is aligned with the percolated microcracks. The crack-opening magnitudes are indicated next to the macrocrack.

In the third column, we show the result of a coarse-graining procedure for the same microcrack configuration with two macrocracks. The evolution of the major macrocrack is unchanged. The minor macrocrack opens substantially less.

6.2. Three-point bending

A coarse-scale model for a boron–aluminum composite is shown in Figure 7(a). The fine-scale model is shown in Figure 7(b); its solution is hereafter referred to as the direct numerical simulation (DNS). The center of the coarse-scale model was linked to identical unit cells, one of which is shown in Figure 7(c). In the unit cell, we explicitly modeled the boron particles and the aluminum matrix so that the volume fraction of the particles is 10%. The boron particles are linear elastic isotropic: $E = 413.0$ GPa and $\nu = 0.20$. For the aluminum matrix, a Lemaitre damage constitutive model [39] was used: $E = 67.50$ GPa and $\nu = 0.36$. Outside the center area in both the coarse- and fine-scale models, the material is linear elastic with an effective elastic modulus which is computed by conventional homogenization theory as $E = 75.60$ GPa and $\nu = 0.35$.

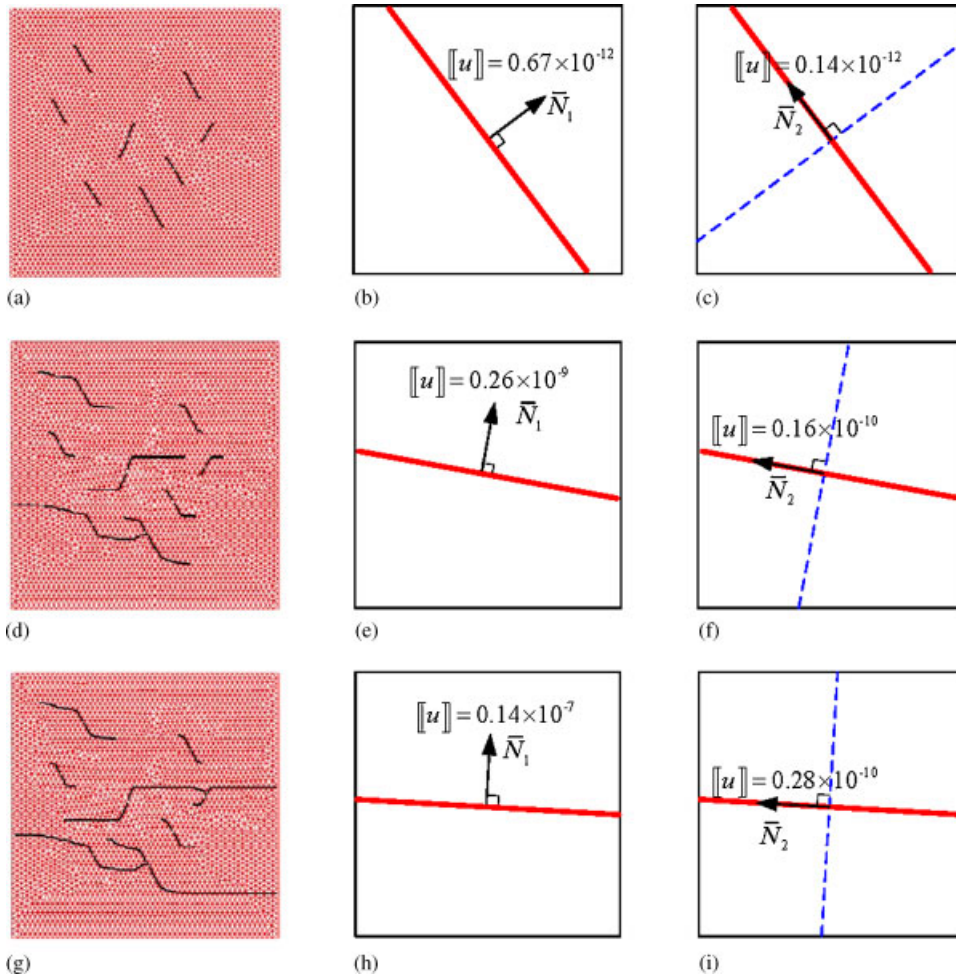


Figure 6. Growth of fatigue cracks in a unit cell (in the first column) and the corresponding coarse-grain discontinuities obtained by Equation (19) (in the second and third columns); major and minor macrocracks are denoted by solid and dashed lines, respectively.

The results were obtained by an explicit dynamic analysis using a sufficiently slow loading rate so that dynamic effects are minimal. However, it should be noted that, regardless of the slowness, snapback will not be apparent in this approach.

Figures 8(a) and (b) show the final configurations of the coarse-scale model and DNS, respectively. As can be seen, the crack path in the DNS is quite irregular due to the microstructure. However, in the coarse-scale simulation, this jaggedness is absent since the resolution of crack path by the coarse model cannot capture these details.

The evolution of a discontinuity in a typical unit cell is shown in Figures 9(a)–(c). As can be seen, the crack starts at the interface of the matrix material with the inclusion, and then progresses to the edges. Neither macro boundary effects nor the effects of adjacent cracks were considered. A typical result for the stress–strain response in terms of the effective strain is shown in Figure 9(d).

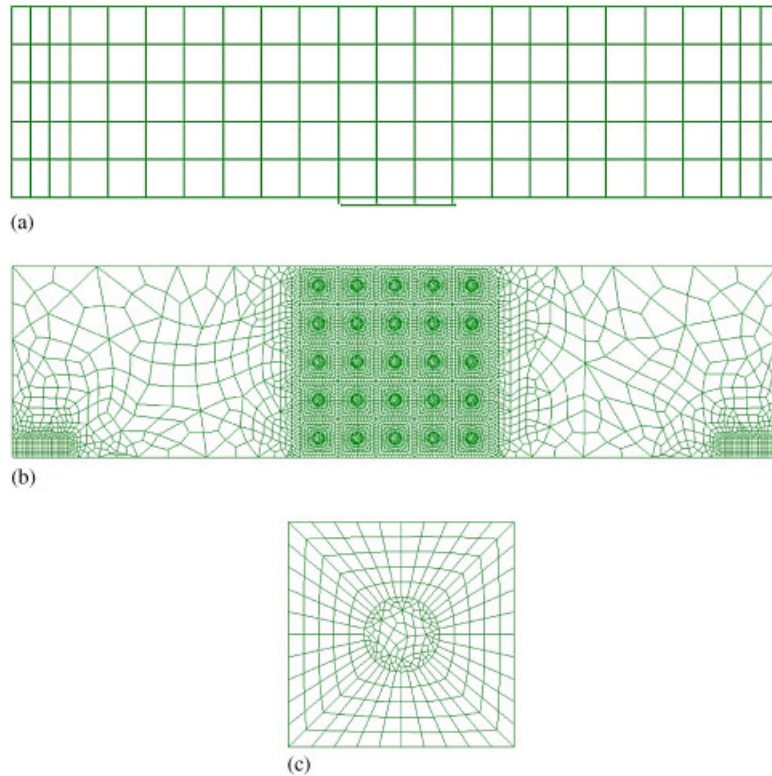


Figure 7. Finite element discretizations for: (a) the multiscale aggregating discontinuities method; (b) direct numerical simulation method; and (c) the unit cell model.

As can be seen, the stress monotonically increases with a decreasing slope until a strain of 1.2%. When the crack opening becomes sufficiently large, the slope becomes negative and discontinuities are inserted in the coarse-scale model as shown in Figure 8(a).

A comparison of the coarse-grain MAD results with DNS is shown in Figure 10. As can be seen, the agreement is quite good; the relative error in the maximum load is 8.3%. At the end of the simulation, a moderate discrepancy emerges. Hence, even though the jaggedness of the crack path is not apparent in the coarse-grain results, it appears to be reflected adequately through the coarse-grained stress–strain law.

7. DISCUSSION AND CONCLUSIONS

Although the method has here been described and implemented in the context of multiscale continuum mechanics, it is especially promising for multiscale models involving discrete models, such as atomistic or the discrete element method (DEM), at the finest scale. An example of such multiscale model is illustrated in Figure 11, where the atomistic model is the finest scale.

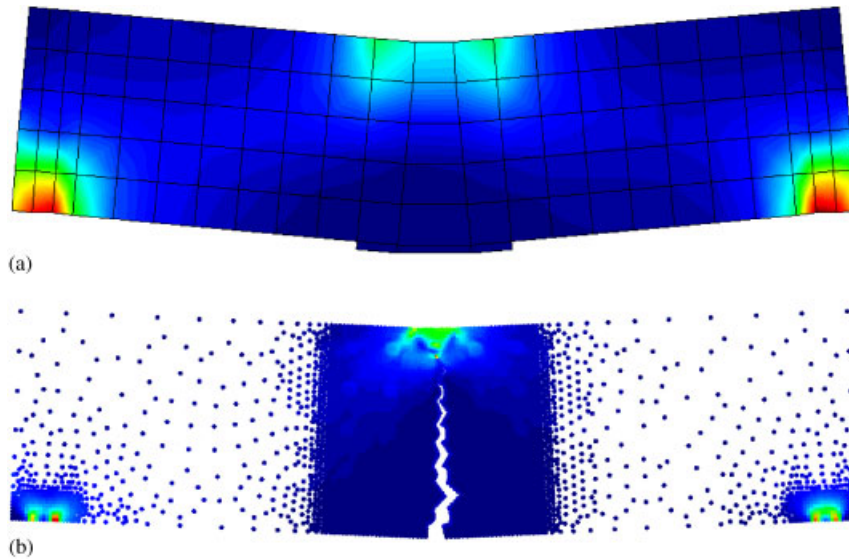


Figure 8. The final configuration of 3-point bending simulations: (a) effective stress plot of the multiscale aggregating discontinuities method; the dashed line represents equivalent crack growth path and (b) effective stress plot of direct numerical simulation; for better resolution on crack opening, only nodal points were plotted.

Obviously, hierarchical models would encounter difficulties in passing from the atomistic scale to the microscale when the former encounters bond breaking, such as in the nucleation of cracks or dislocations, because the tangent stiffness matrix of the atomistic unit cell may then lose positive definiteness. Consequently, the constitutive response that is passed from the atomistic model (this model may be called AtC^2 : atomistic to continuum to continuum) is not stable, and the coarser-scale model is not well posed.

In the MAD method, the breaking bonds are excluded from the perforated unit cell, and, as shown in Section 4, the response of the bulk material at the coarser scale would be stable. The effect of the unstable behavior at the atomistic scale is passed to the coarser scale by the injected discontinuity; both the magnitude of the displacement jump at the coarser scale and the direction of the discontinuity are provided by the unit cell. In the case of an edge dislocation, once it is fully developed, the jump would be the Burgers vector. In the case of the nucleation of a crack at the atomic scale, the magnitude of the jump discontinuity would be governed by coarse-scale equilibrium once the crack is fully developed in the unit cell. The appropriateness of this approach is readily apparent. Cracks are almost always treated as discontinuities in continuum models. Similarly, dislocations are usually implicitly treated as discontinuities. In the image field methods of Van der Giessen and Needleman [40], the discontinuities appear in the superimposed closed-form solutions, whereas in the Green's function methods of Amodeo and Ghoniem [41] and Bulatov and Cai [42], the discontinuities are implicit in the Green's functions solution. In the method of Gracie *et al.* [43], dislocations are treated explicitly as discontinuities in the sense of Volterra. Although cracks and dislocations can be regularized (i.e. smeared), such methods entail far bigger models and information passing may be more difficult.

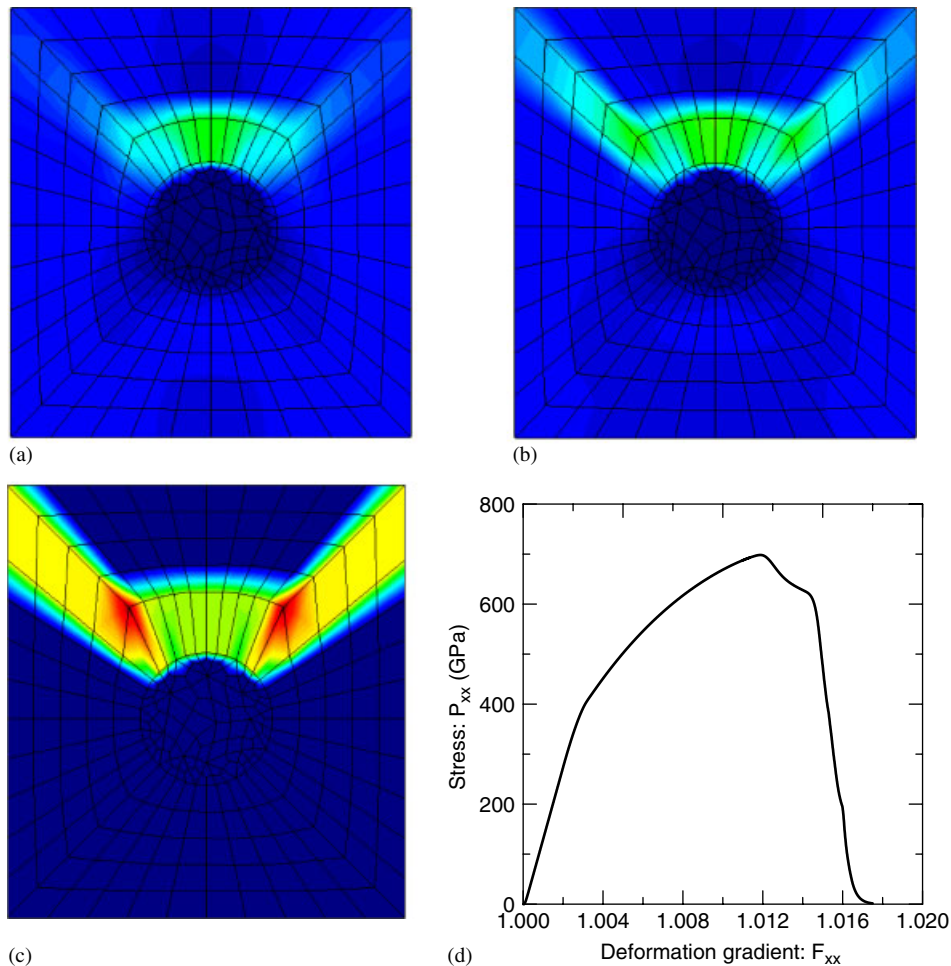


Figure 9. The evolution of discontinuity in a typical unit cell is rotated by 90° : (a) initial stage; (b) intermediate stage; (c) final stages; and (d) a typical stress–strain behavior of the unit cell.

If the intermediate scale has a rich microstructure that is beyond the reach of homogenization methods, coarse graining up to the next scale can be performed similarly. Of course, such two-level coarse graining will require tremendous computational resources, but the imminent petaflop computers will be able to deal with such models. Furthermore, the expense can be reduced substantially by limiting the MAD approach to ‘hot spots’ or by using the neural networks as described previously.

A key feature of this work is the method for extracting a single discontinuity from the unit cell to be injected at the coarser scale. Both the orientation of the discontinuity and the displacement jump magnitude are determined by this method. For unit cells where the cracks and localization bands are not aligned along a predominant direction, a method for extracting additional discontinuities has also been described.

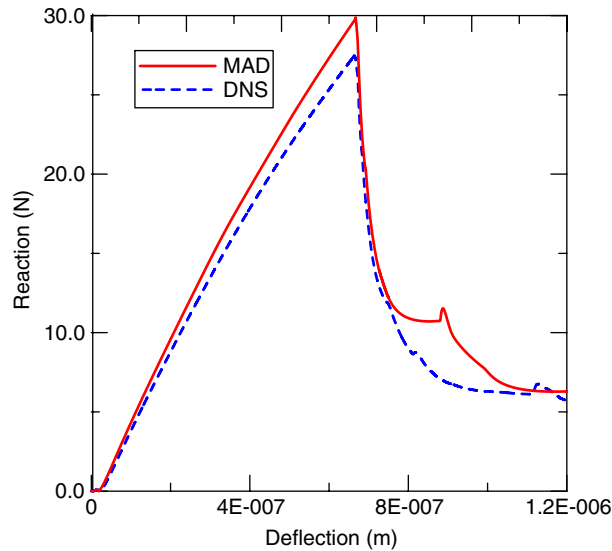


Figure 10. Comparison of load–deflection curve between the multiscale aggregating discontinuities method and direct numerical simulation.

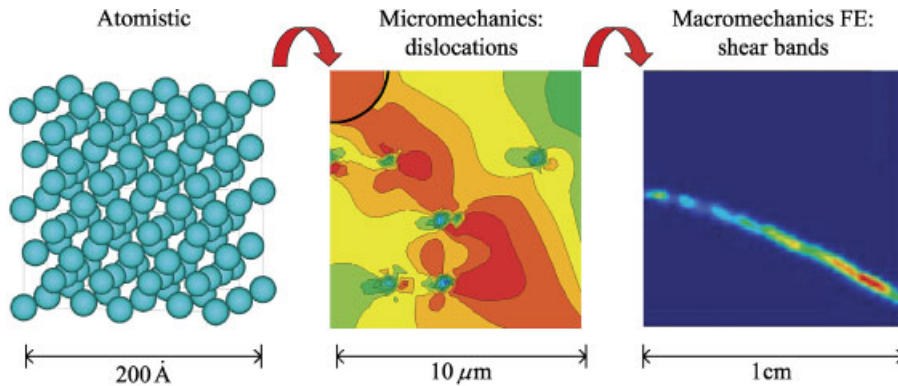


Figure 11. Potential application of the multiscale aggregating discontinuities method: atomistic to dislocations to shear bands.

It could be argued that the proposed method offers little advantage over concurrent analysis at different scales, such as in Xiao and Belytschko [44], Wagner and Liu [45] or Karpov *et al.* [46], and this argument cannot be dismissed lightly. If MAD were to be used without the various ways of reducing computational expense, such as neural networks and invocation only at hot spots, then its advantage over concurrent analysis is not clear. However, in addition to computational efficiencies that will accrue due to exploiting techniques such as neural networks, several advantages over concurrent analysis are readily apparent:

- (i) The conditioning of the equations is improved (the large ratio of element sizes in the macro model to those in the unit cell would substantially impair conditioning).

- (ii) In explicit methods, subcycling is avoided.
- (iii) Parallel implementations are more straightforward because little information is passed between the scales (in concurrent methods, information for all nodes on the boundary must be passed).

The MAD method is still quite embryonic, and many difficulties remain to be resolved. For example, the application of boundary conditions on the unit cell and information transfer to/from the unit cell pose several difficulties, and we have not overcome all of them to our satisfaction. Among these, difficulties and needed developments are the following:

- (i) When the unit cell localizes, prescribed linear displacements as given in the analysis are not compatible with the discontinuities; this has been discussed in Section 3.
- (ii) It would be desirable to model a discontinuity that varies linearly in the unit cell.
- (iii) The effects of boundaries and adjacent discontinuities are not reflected in the method.

The first difficulty can be ameliorated by using prescribed traction boundary conditions. This approach is also more consistent with the neural network strategy that we have discussed. Including the effects of the environment on the unit cell, such as adjacent boundaries and adjacent discontinuities, poses no fundamental difficulties, but it will entail additional complexity in the programming and some fundamental improvements in the strategy for injecting discontinuities.

As can be seen, the impediments to the full realization of the potentials of this method are primarily technical, i.e. in the details. The proposed method overcomes a fundamental barrier in the application of hierarchical multiscale methods, i.e. coarse graining, to problems of failure, for it enables one to coarse grain the bulk response so that it remains stable. This makes possible a numerically sound and robust treatment of failure problems by multiscale methods.

APPENDIX A

Consider a unit cell of constant area in one dimension with n cohesive cracks as shown in Figure A1. In reality, this situation would be highly unlikely, since in a symmetric configuration such as this, the largest imperfection would break symmetry and prevent failure at a second imperfection. However, we examine this case since it sheds some light on the relation between element size and unit cell size.

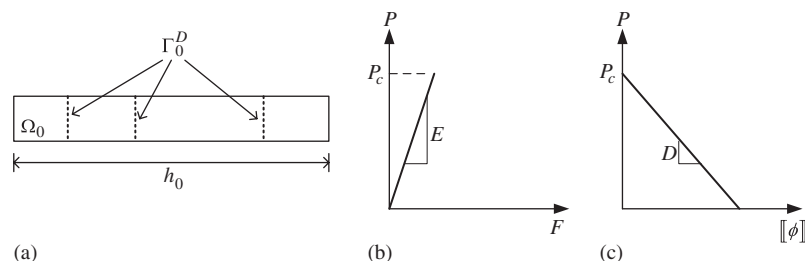


Figure A1. Unit cell for the dimensional cracking problem showing: (a) a domain with three cracks; (b) the stress–strain curve of the pristine material; and (c) the traction–displacement jump relation.

The material is linear elastic with Young’s modulus E and a fracture stress P_c so that

$$P^K(X, t) = E^K F^K(X, t) \quad \text{if } P(X, \bar{t}) < P_c \quad \forall \bar{t} < t \tag{A1}$$

$$P^K(X, t) = P_c - D \llbracket \phi^K(X) \rrbracket \quad \text{if } P(X, t) = P_c \text{ for some } \bar{t} < t \tag{A2}$$

It is assumed that $\llbracket \phi \rrbracket \geq 0$. The original length of the unit cell is h_0 and its original cross-sectional area is unity.

The average strain F^K is given by

$$h_0 \langle F^K \rangle = \int_{\Omega_0 \setminus \Gamma_0^D} F^K \, dX = \underbrace{\phi^K(X_2) - \phi^K(X_1)}_{\mathcal{F}^{K-1}} - \sum_{J=1}^n \llbracket \phi^k(X_J) \rrbracket \tag{A3}$$

The above is the counterpart of Equation (16).

In one dimension, the stress must be constant by equilibrium so that $h_0 \langle P^K(X) \rangle = P^K = E^k F^k = P^{K-1}$. Otherwise, $P^{K-1} = P^k = P_c - nD \llbracket \phi^K \rrbracket$ since all cracks must open by an equal amount.

Rewriting Equation (A3) in terms of the stress gives

$$\int_{\Omega_0 \setminus \Gamma_0^D} \frac{P^K}{E^K} \, dX = \underbrace{(\phi_2 - \phi_1)}_{\delta} - n \frac{P_c - P^K}{D} \tag{A4}$$

or

$$P^{K-1} \left(\frac{h_0}{E^K} - \frac{n}{D} \right) = \delta - \frac{nP_c}{D} \tag{A5}$$

where we have used $P^K = P^{K-1}$. The quantity in parentheses is the inverse of the tangent stiffness of the unit cell. It is easy to verify that it (and the tangent stiffness) is positive when $E/D > h_0/n$, but otherwise it is negative and the unit cell snaps back.

It also becomes clear that the size of the unit cell must be equal to element size; otherwise the number of cracks in the unit cell and hence the response are incorrect. In the strain-softening branch, the tangent stiffness of the unit cell depends linearly on the number of cracks and the size of domain.

In the post-critical regime, the bulk relationship, P^{K-1} vs F^{K-1} , is obtained by subtracting the effect of the discontinuities in Equation (A4), yielding

$$\frac{h_0 P^K}{E^K} = F^K h_0 \tag{A6}$$

Thus, the bulk response remains stable.

The power \dot{W} at the coarse scale and fine scale are given, respectively, by

$$\dot{W}^{K-1} = P^{K-1} \dot{\mathcal{F}}^{K-1} \tag{A7}$$

$$\dot{W}^K = \int_{\Omega_0 \setminus \Gamma_0^D} P^K \dot{F}^K \, dX + \sum_J P^K \llbracket \dot{\phi}(X_J) \rrbracket \tag{A8}$$

From (A3), we can see that $\dot{\mathcal{F}}^{K-1} = \dot{\phi}_2 - \dot{\phi}_1$. So recalling that $P^{K-1} = P^K$, it follows that

$$\dot{W}^{K-1} = P^K (\dot{\phi}_2 - \dot{\phi}_1) \tag{A9}$$

Since $P^K(X)$ denoted by P^K , is constant, by equilibrium

$$\begin{aligned} \dot{W}^K &= P^K \left(\int_{\Omega_0 \setminus \Gamma_0^D} \dot{F}^K \, dX + \sum_J \llbracket \phi(X_J) \rrbracket \right) \\ &= P^K (\dot{\phi}_2 - \dot{\phi}_1) \end{aligned} \tag{A10}$$

Comparing Equations (A9) and (A10), we can see that the power at the two scales is equivalent.

APPENDIX B

To compute the orientation, $\bar{\mathbf{N}}$, and the magnitude, $\bar{\mathbf{U}}$, of a coarse-grained equivalent discontinuity, we need to solve the unconstrained multivariable minimization problem that is stated in Equation (19). In this Appendix, we will show a simple algebraic solution for the problem, which is valid for a two-dimensional case.

Denote by J the function $J = (\bar{\mathbf{U}} \otimes \bar{\mathbf{N}} - \mathbf{F}_E)^2$. To find the minimum of J , we need to find $\bar{\mathbf{U}}$ and $\bar{\mathbf{N}}$ such that

$$\frac{\partial J}{\partial \bar{U}_i} = \frac{\partial J}{\partial \bar{N}_j} = 0 \tag{B1}$$

Note that, in the two-dimensional case, $\bar{\mathbf{N}} = [\cos \theta \ \sin \theta]^T$ and $\|\bar{\mathbf{N}}\| = 1$.

Writing the function J in indicial notation yields

$$\begin{aligned} J &= (\bar{U}_i \bar{N}_j - F_{ij}^E)(\bar{U}_i \bar{N}_j - F_{ij}^E) \\ &= \left(\underbrace{\bar{U}_i \bar{U}_i \bar{N}_j \bar{N}_j}_{=1} - 2\bar{U}_i \bar{N}_j F_{ij}^E + F_{ij}^E F_{ij}^E \right) \end{aligned} \tag{B2}$$

By substituting Equation (B2) into (B1), we obtain a set of two equations:

$$\frac{\partial J}{\partial \bar{U}_k} = 2\bar{U}_k - 2F_{kj}^E \bar{N}_j = 0 \tag{B3}$$

$$\frac{\partial J}{\partial \bar{N}_k} = F_{ik}^E \bar{U}_i \frac{\partial \bar{N}_k}{\partial \theta} = 0 \tag{B4}$$

Substituting Equation (B3) into (B4):

$$\underbrace{F_{ik}^E F_{ij}^E}_{C_{jk}} \bar{N}_j \frac{\partial \bar{N}_k}{\partial \theta} = 0 \tag{B5}$$

which in two dimensions yields a single algebraic equation:

$$C_{12} \cos^2 \theta - C_{21} \sin^2 \theta - (C_{11} - C_{22}) \cos \theta \sin \theta = 0 \tag{B6}$$

From Equation (B6), we can easily compute the orientation $\bar{\mathbf{N}}$ in terms of θ and then by substituting the value into Equation (B3) we can compute the equivalent discontinuity magnitude $\bar{\mathbf{U}}$.

Note added in proof: We just became aware of another approach to introducing discontinuities in multiscale methods, Reference [47].

ACKNOWLEDGEMENTS

The support of the Army Office of Scientific Research under Grant W911-NF-05-1-0049 and the Office of Naval Research under Grant N00014-06-1-0380 is gratefully acknowledged. We thank Tarek I. Zohdi for his valuable discussions.

REFERENCES

1. Feyel F, Chaboche JL. FE² multiscale approach for modelling the elastoviscoplastic behaviour of long fibre SiC/Ti composite materials. *Computer Methods in Applied Mechanics and Engineering* 2000; **183**:309–330.
2. Feyel F. A multilevel finite element method (FE²) to describe the response of highly non-linear structures using generalized continua. *Computer Methods in Applied Mechanics and Engineering* 2003; **192**:3233–3244.
3. Kouznetsova V, Geers MGD, Brekelmans WAM. Multi-scale constitutive modelling of heterogeneous materials with a gradient-enhanced computational homogenization scheme. *International Journal for Numerical Methods in Engineering* 2002; **54**:1235–1260.
4. McVeigh C, Vermeire F, Liu WK, Moran B, Olson G. An interactive micro-void shear localization mechanism in high strength steels. *Journal of the Mechanics and Physics of Solids* 2007; **55**:225–244.
5. Gitman IM. Representative volumes and multi scale modelling of quasi brittle materials. *Ph.D. Dissertation*, Technical University Delft, 2006.
6. Gitman IM, Askes H, Aifantis EC. The representative volume size in static and dynamic micro–macro transitions. *International Journal of Fracture* 2005; **135**:L3–L9.
7. Oskay C, Fish J. Eigendeformation-based reduced order homogenization for failure analysis of heterogeneous materials. *Computer Methods in Applied Mechanics and Engineering* 2007; **196**:1216–1243.
8. Bažant ZP, Belytschko T, Chang TP. Continuum theory for strain-softening. *Journal of Engineering Mechanics (ASCE)* 1984; **110**(12):1666–1692.
9. Triantafyllidis N, Aifantis EC. A gradient approach to localization of deformation: 1. hyperelastic materials. *Journal of Elasticity* 1986; **16**:225–237.
10. Lasry D, Belytschko T. Localization limiters in transient problems. *International Journal of Solids and Structures* 1988; **24**(6):581–597.
11. Bažant ZP, Belytschko T. Wave propagation in a strain-softening bar: exact solution. *Journal of Engineering Mechanics (ASCE)* 1985; **111**(3):381–389.
12. Belytschko T, Banžant ZP, Hyun YW, Chang TP. Strain-softening materials and finite-element solutions. *Computers and Structures* 1986; **23**:163–180.
13. Fleck NA, Hutchinson JW. A phenomenological theory for strain gradient effects in plasticity. *Journal of the Mechanics and Physics of Solids* 1993; **41**:1825–1857.
14. Fleck NA, Hutchinson JW. A reformulation of strain gradient plasticity. *Journal of the Mechanics and Physics of Solids* 2001; **49**:2245–2271.
15. Gao H, Huang Y, Nix WD, Hutchinson JW. Mechanism-based strain gradient plasticity—I. Theory. *Journal of the Mechanics and Physics of Solids* 1999; **47**:1239–1263.
16. Abeyaratne R, Triantafyllidis N. An investigation of localization in a porous elastic material using homogenization theory. *Journal of Applied Mechanics (ASME)* 1984; **51**:481–486.
17. Geymonat G, Müller S, Triantafyllidis N. Homogenization of nonlinearly elastic materials, microscopic bifurcation and macroscopic loss of rank-one convexity. *Archive for Rational Mechanics and Analysis* 1993; **122**:231–290.
18. Müller S. Homogenization of nonconvex integral functionals and cellular elastic materials. *Archive for Rational Mechanics and Analysis* 1987; **99**:189–212.
19. Miehe C, Schröder J, Becker M. Computational homogenization analysis in finite elasticity: material and structural instabilities on the micro- and macro-scales of periodic composites and their interaction. *Computer Methods in Applied Mechanics and Engineering* 2002; **191**:4971–5005.
20. Belytschko T, Liu WK, Moran B. *Nonlinear Finite Elements for Continua and Structures*. Wiley: New York, 2000.

21. Moës N, Dolbow J, Belytschko T. A finite element method for crack growth without remeshing. *International Journal for Numerical Methods in Engineering* 1999; **46**(1):131–150.
22. Belytschko T, Moës N, Usui S, Parimi C. Arbitrary discontinuities in finite elements. *International Journal for Numerical Methods in Engineering* 2001; **50**(4):993–1013.
23. Fries TP, Belytschko T. The intrinsic XFEM: a method for arbitrary discontinuities without additional unknowns. *International Journal for Numerical Methods in Engineering* 2006; **68**:1358–1385.
24. Menouillard T, Réthoré J, Combescure A, Bung H. Efficient explicit time stepping for the extended finite element method. *International Journal for Numerical Methods in Engineering* 2006; **68**:911–939.
25. Song J-H, Areias PMA, Belytschko T. A method for dynamic crack and shear band propagation with phantom nodes. *International Journal for Numerical Methods in Engineering* 2006; **67**:868–893.
26. Xiao QZ, Karihaloo BL, Liu XY. Incremental-secant modulus iteration scheme and stress recovery for simulating cracking process in quasi-brittle materials using XFEM. *International Journal for Numerical Methods in Engineering* 2007; **69**:2606–2635.
27. Asadpoure A, Mohammadi S. Developing new enrichment functions for crack simulation in orthotropic media by the extended finite element method. *International Journal for Numerical Methods in Engineering* 2007; **69**:2150–2172.
28. Prabel B, Combescure A, Gravouil A, Marie S. Level set X-FEM non-matching meshes: application to dynamic crack propagation in elastic–plastic media. *International Journal for Numerical Methods in Engineering* 2007; **69**:1553–1569.
29. Rabczuk T, Areias PMA, Belytschko T. A simplified meshfree method for shear bands with cohesive surfaces. *International Journal for Numerical Methods in Engineering* 2007; **69**:993–1021.
30. Furukawa T, Yagawa G. Implicit constitutive modelling for viscoplasticity using neural networks. *International Journal for Numerical Methods in Engineering* 1998; **43**:195–219.
31. Yun GJ, Ghaboussi J, Elnashai AS. A new neural network-based model for hysteretic behavior of materials. *International Journal for Numerical Methods in Engineering* 2007; DOI: 10.1002/nme.2082.
32. Zohdi TI, Wriggers P. *Introduction to Computational Micromechanics*. Lecture Notes in Applied and Computational Mechanics, vol. 20. Springer: Berlin, 2005.
33. Nemat-Nasser S, Hori M. *Micromechanics: Overall Properties of Heterogeneous Solids* (2nd edn). Elsevier: Amsterdam, New York, 1999.
34. Loehnert S. Computational homogenization of microheterogeneous materials at finite strains including damage. *Ph.D. Thesis*, University Hannover, 2004.
35. Zohdi T. Personal communication.
36. Flanagan DP, Belytschko T. A uniform strain hexahedron and quadrilateral with orthogonal hourglass control. *International Journal for Numerical Methods in Engineering* 1981; **17**:679–706.
37. Belytschko T, Ong JSJ, Liu WK, Kennedy JM. Hourglass control in linear and nonlinear problems. *Computer Methods in Applied Mechanics and Engineering* 1984; **43**(3):251–276.
38. Belytschko T, Bachrach WE. Efficient implementation of quadrilaterals with high coarse-mesh accuracy. *Computer Methods in Applied Mechanics and Engineering* 1986; **54**:279–301.
39. Lemaître J, Chaboche JL. *Mechanics of Solid Materials*. Cambridge University Press: Cambridge, 1990. ISBN 0-521-32853-5.
40. Van der Giessen E, Needleman A. Discrete dislocation plasticity: a simple planar model. *Modelling Simulation in Material Science and Engineering* 1995; **3**:689–735.
41. Amodeo RJ, Ghoniem NM. Dislocation dynamics. I. A proposed methodology for deformation micromechanics. *Physical Review B* 1990; **41**:6958–6967.
42. Bulatov V, Cai W. *Computer Simulations of Dislocations*. Oxford Series on Materials Modelling. Oxford University Press: Oxford, New York, 2006.
43. Gracie R, Ventura G, Belytschko T. A new fast finite element method for dislocations based on interior discontinuities. *International Journal for Numerical Methods in Engineering* 2007; **69**:423–441.
44. Xiao SP, Belytschko T. A bridging domain method for coupling continua with molecular dynamics. *Computer Methods in Applied Mechanics and Engineering* 2004; **193**:1645–1669.
45. Wagner GJ, Liu WK. Coupling of atomistic and continuum simulations using a bridging scale decomposition. *Journal of Computational Physics* 2003; **190**:249–274.
46. Karpov EG, Park HS, Liu WK. A phonon heat bath approach for the atomistic and multiscale simulation of solids. *International Journal for Numerical Methods in Engineering* 2007; **70**:351–378.
47. Massart TJ, Peerlings RHJ, Geers MGD. An enhanced multi-scale approach for masonry wall computations with localization of damage. *International Journal for Numerical Methods in Engineering* 2007; **69**(5):1022–1059.